

PAPER • OPEN ACCESS

## A high sensitivity wide bandwidth spectral system for multiple K-edge imaging

To cite this article: P Perion *et al* 2024 *J. Phys. D: Appl. Phys.* **57** 355402

View the [article online](#) for updates and enhancements.

You may also like

- [Development and validation of an iodine plasma model for gridded ion thrusters](#)  
T Lafleur, L Habl, E Zorzoli Rossi et al.
- [Ion plume investigation of a Hall effect thruster operating with Xe/N<sub>2</sub> and Xe/air mixtures](#)  
Antonio Gurciullo, Andrea Lucca Fabris and Mark A Cappelli
- [Determination and analysis of plasma parameters for simulations of radiative blast waves launched in clusters of xenon and krypton](#)  
R Rodriguez, J M Gil, G Espinosa et al.

**PRIME**  
PACIFIC RIM MEETING  
ON ELECTROCHEMICAL  
AND SOLID STATE SCIENCE




**HONOLULU, HI**  
October 6-11, 2024

*Joint International Meeting of*  
The Electrochemical Society of Japan  
(ECS)  
The Korean Electrochemical Society  
(KECS)  
The Electrochemical Society (ECS)

Early Registration Deadline:  
**September 3, 2024**

**MAKE YOUR PLANS  
NOW!**

# A high sensitivity wide bandwidth spectral system for multiple K-edge imaging

P Perion<sup>1,2</sup> , L Brombal<sup>1,2,\*</sup> , P Delogu<sup>3,4</sup>, V di Trapani<sup>1</sup>, R H Menk<sup>2,5,6</sup>, P Oliva<sup>7,8</sup>  and F Arfelli<sup>1,2</sup>

<sup>1</sup> Department of Physics, University of Trieste, Trieste, Italy

<sup>2</sup> Division of Trieste, Istituto Nazionale di Fisica Nucleare, Trieste, Italy

<sup>3</sup> Department of Physical Science, Earth and Environment, University of Siena, Siena, Italy

<sup>4</sup> Division of Pisa, Istituto Nazionale di Fisica Nucleare, Pisa, Italy

<sup>5</sup> Elettra Sincrotrone Trieste, Trieste, Italy

<sup>6</sup> Department of Computer and Electrical Engineering, Mid Sweden University, Sundsvall, Sweden

<sup>7</sup> Department of Chemical, Physical, Mathematical and Natural Sciences, University of Sassari, Sassari, Italy

<sup>8</sup> Division of Cagliari, Istituto Nazionale di Fisica Nucleare, Cagliari, Italy

E-mail: [luca.brombal@ts.infn.it](mailto:luca.brombal@ts.infn.it)

Received 22 December 2023, revised 19 April 2024

Accepted for publication 23 May 2024

Published 6 June 2024



CrossMark

## Abstract

Spectral K-edge subtraction (SKES) is an imaging technique that takes advantage of the sharp rise in the mass attenuation coefficient of specific elements within an object at their K-edge to produce separate and quantifiable distributions of each element. In this paper, a high-sensitivity and wide bandwidth SKES imaging system for computed tomography applications on biological samples is presented. X-ray images are acquired using a wide and continuous energy spectrum that encompasses the absorption edges of the target materials. System characterization shows that high energy resolution (approximately  $3 \times 10^{-3}$ ) and unprecedented large energy bandwidth (around 15%) are achieved over a field-of-view of several centimeters. Imaging results obtained on contrast elements relevant for biomedical applications, namely silver, iodine, xenon, and barium, demonstrate the system sensitivity to concentrations down to  $0.5 \text{ mg ml}^{-1}$ . The achievement of a large energy bandwidth allowed the simultaneous imaging of the K-edges of iodine, xenon, and barium and provided an accurate concentration estimation and distinction of co-localized contrast elements, leading the way for future simultaneous cardiovascular (iodine), pulmonary (xenon), and gastrointestinal/inflammatory (barium) imaging applications.

Keywords: spectral x-ray imaging, spectral tomography, multiple K-edge, energy dispersive Laue

\* Author to whom any correspondence should be addressed.



Original Content from this work may be used under the terms of the [Creative Commons Attribution 4.0 licence](https://creativecommons.org/licenses/by/4.0/). Any further distribution of this work must maintain attribution to the author(s) and the title of the work, journal citation and DOI.

## 1. Introduction

Spectral x-ray imaging is an imaging method whose aim is to obtain information about the chemical composition of an object by exploiting the energy dependence of x-ray photon attenuation in matter. This procedure requires the images to be acquired at multiple (at least two) x-ray energies, and it can discriminate among different materials/compounds within an object providing quantitative and material-specific maps (Vries *et al* 2014, Fredenberg 2018).

High-atomic-number contrast agents are being used in biomedical x-ray imaging applications to enhance the contrast of otherwise scarcely visible target tissues or structures within the body. When combined with spectral x-ray imaging, the use of contrast elements greatly improves material differentiation and quantification by exploiting the element absorption edges, further increasing the visibility of details of interest (Panahifar *et al* 2016, Panta *et al* 2018).

In the past decades, many spectral imaging techniques employing x-rays have been introduced. Spectral scanners used in medical applications typically use a ‘spectrum-based’ approach, where two images are acquired at two different energy levels, either by producing two different x-ray spectra during the acquisition (dual-energy), or by detecting different spectral components through a layered detector (Altman and Carmi 2009, Fredenberg 2018). More recently, single-shot ‘detector-based’ spectral imaging has become a viable option, due to the advent of pixellated hybrid detectors equipped with high-Z sensors, where the incoming photons can be grouped into two (or more) energy bins (Ballabriga *et al* 2016). The latter approach brings a major simplification in the imaging system and an improvement in flexibility. Detector-based spectral computed tomography (CT) scanners are now becoming commercially available in hospitals (Rajendran *et al* 2022), while several examples of integration of small-pixel (<100  $\mu\text{m}$ ) spectral detectors within micro-CT systems have been recently published (Badea *et al* 2019, Brun *et al* 2020, Brombal *et al* 2023).

In this context, an additional high-sensitivity large-bandwidth spectral imaging method is the crystal-based spectral K-edge subtraction (SKES) (Zhu *et al* 2014). SKES is a synchrotron-based imaging technique that exploits the sharp rise of the mass attenuation coefficient at the K-edge energy of specific elements, either purposely inserted or naturally present in the sample. SKES can be considered as an evolution of the KES imaging technique, where two images, taken at energies above and below the target element K-edge, are subtracted logarithmically (Rubenstein 1984, Thomlinson *et al* 2018). Unlike KES, SKES involves the acquisition of x-ray images on a continuous and spatially dispersed energy spectrum containing the contrast medium K-edge energy (i.e. K-edge bracketing). The spectrum, which will from now on be referred to as energy bandwidth, is prepared from a polychromatic x-ray beam, produced by a synchrotron source, traversing a cylindrically bent Laue (i.e. transmission-type) crystal that acts as a monochromator (Qi *et al* 2021). Owing to the curvature of the crystal, the diffracted beam is geometrically

focused onto a line and energetically dispersed in the diffraction plane, being collected by a 2D pixelated detector. The diffracted energies are vertically mapped onto different pixel rows along the diffraction plane. Consequently, the acquisition is performed utilizing an energy bandwidth which comprises tens to hundreds of energy bins, also opening up the possibility of imaging multiple K-edges simultaneously (Bassey *et al* 2016).

Crystal-based KES systems have been used in a number of biomedical imaging applications (Thomlinson *et al* 2018), e.g. in the field of coronary angiography (Bertrand *et al* 2005) and lung imaging (Bayat *et al* 2001). Compared to KES, the advent of SKES has the potential to improve results in terms of sensitivity, but also to pave the way for new applications making use, for instance, of multiple contrast agents to target different anatomical or functional districts.

In the implementation of a SKES setup, both the diffracted spectrum bandwidth and the energy resolution are fundamental parameters defining the overall imaging performance. When pursuing multiple K-edge imaging, the spectral bandwidth ultimately determines the number and the type of contrast media that can be simultaneously imaged. Once the geometrical and crystal parameters have been fixed, the spectral bandwidth is found to be inversely proportional to the bending radius, whose lower bound (i.e. maximum bending) corresponds to the rupture of the crystal itself. On the other hand, energy resolution measures the quality of the energetic spatial dispersion, which in turn determines the blur of the detected K-edge along the energy axis. A large energy blurring negatively affects the material decomposition as a relevant portion of the field-of-view is occupied by edge-crossing energies (Samadi *et al* 2016). Additionally, a poor energy resolution does not allow the detection of subtle near-edge attenuation features, thus preventing the implementation of near-edge spectroscopy techniques such as EXAFS (Qi *et al* 2019). In general, the energy resolution of a bent Laue crystal depends on several parameters including the reflection type, the lattice  $d$ -spacing variation across the crystal due to its curvature, beam divergence, and the effect of the finite source size (Qi *et al* 2021). Nonetheless, it has been demonstrated that by choosing asymmetrically cut crystals matching a focusing criterion referred to as *magic condition* (Martinson *et al* 2015, Qi *et al* 2021) optimal energy resolution can be reached. The understanding of the magic condition has paved the way for SKES, bringing a significant reduction of edge-crossing energies (from around 30% to a few % of the field-of-view), and removing the need for beam splitters (Samadi *et al* 2016).

In this context, the present work reports on a SKES imaging setup featuring, to the best of the authors’ knowledge, the largest energy bandwidth along the direction orthogonal to the plane of the laminar beam reported so far coupled to a large field of view (FOV) (several cm).

The spectral system is characterized in terms of both energy bandwidth and resolution at energies corresponding to K-edges of contrast media relevant for biomedical imaging, namely silver, iodine, xenon, and barium. The capability of performing simultaneous SKES tomographic imaging of

iodine, xenon, and barium over a FOV of several centimeters is being demonstrated for the first time. For each contrast element, the quantitiveness and sensitivity of the system are evaluated on tomographic images of test samples containing multiple contrast media dilutions. The experimental setup was implemented at the SYRMEP beamline of the synchrotron facility Elettra (Trieste, Italy) in the context of the INFN (National Institute of Nuclear Physics) research projects KISS (K-edge Imaging at Synchrotron Sources) and SPHERE-X (Spectral PHAsE REtrieval x-ray imaging).

## 2. Materials and methods

### 2.1. Experimental setup

The imaging study was performed at the SYRMEP beamline at Elettra operated in the white-beam mode (Tromba *et al* 2010) by using the setup shown in figure 1. The energy dispersion of the beam was achieved by employing a 750  $\mu\text{m}$  thick Si wafer featuring a 3-degree asymmetrical cut with respect to the selected (111) diffraction plane. The wafer was bent to a radius of 0.5 m through a custom-designed two-bar bender, shown in the inset of figure 1(b). The latter consists of two frames: the first one is an aluminum block with a slotted aperture (8 mm  $\times$  80 mm), machined along the bending direction to the desired radius. On the curved surface, a 1 mm thick nylon layer is attached to ensure a more homogeneous stress distribution on the crystal. The second frame consists of an aluminum block featuring a wide aperture and two Teflon rods. The crystal is positioned on the curved frame while the second frame is placed on top and coupled to the first by using two screws. The pressure applied from the rods causes the crystal to bend, making it adhere to the curved surface. The bending frame is positioned onto a 6 degrees-of-freedom hexapod positioning stage located at approximately 23 m downstream from the bending magnet source. Samples are mounted on a dedicated stage comprising a second hexapod, a vertical translator, and a rotator enabling radiographic and tomographic imaging, respectively. Samples are positioned at the focus, namely at 24.7 cm downstream of the crystal. Images were collected with the PIXIRAD-8 CdTe photon-counting detector (Bellazzini *et al* 2013, Delogu *et al* 2016), whose sensitive area is divided into 8 modules, each of 30.7  $\times$  24.8 mm, tiled up to a total sensitive area of 246  $\times$  24.8 mm. The 650  $\mu\text{m}$  thick CdTe sensor ensures high efficiency over a wide range of photon energies, up to 100 keV. Detector pixels are arranged on a hexagonal matrix with 60  $\mu\text{m}$  pitch. The detector is positioned at 80.5 cm from the crystal focus along the diffracted beam direction and mounted onto a manually adjustable tilt platform in order for its sensitive area to be perpendicular to the beam.

### 2.2. Samples

To assess the system's performance, multiple dedicated samples were prepared. Each sample consisted of different sets of plastic cuvettes, filled with a solution of water and a contrast element in different concentrations. The cuvettes were

arranged on a dedicated holder. Concentrations were selected ranging from values typically encountered in biomedical imaging applications that make use of contrast media ( $\geq 10$  mg ml<sup>-1</sup>), down to extremely small values ( $< 1$  mg ml<sup>-1</sup>), to test the detectability limit of the system.

Four different sets of CT images were acquired, each using a different sample:

- i. A silver sample, consisting of seven cuvettes containing silver solutions with concentration 25.0 mg ml<sup>-1</sup>, 10.0 mg ml<sup>-1</sup>, 5.0 mg ml<sup>-1</sup>, 2.5 mg ml<sup>-1</sup>, 1.0 mg ml<sup>-1</sup>, 0.5 mg ml<sup>-1</sup>, 0.0 mg ml<sup>-1</sup> (water only).
- ii. An iodine sample, consisting of seven cuvettes containing iodine solutions with concentration 25.0 mg ml<sup>-1</sup>, 10.0 mg ml<sup>-1</sup>, 5.0 mg ml<sup>-1</sup>, 2.5 mg ml<sup>-1</sup>, 1.0 mg ml<sup>-1</sup>, 0.5 mg ml<sup>-1</sup>, 0.0 mg ml<sup>-1</sup> (water only).
- iii. A barium sample, consisting of seven cuvettes containing barium solutions with concentration 28.1 mg ml<sup>-1</sup>, 11.2 mg ml<sup>-1</sup>, 5.6 mg ml<sup>-1</sup>, 1.1 mg ml<sup>-1</sup>, 0.6 mg ml<sup>-1</sup>, 0.0 mg ml<sup>-1</sup> (water only), and an empty cuvette (0.0 mg ml<sup>-1</sup>).
- iv. A mixed sample, containing three contrast elements, i.e. iodine, xenon, and barium, consisting of five cuvettes. Three of these contained single contrast elements: iodine with concentration 10.0 mg ml<sup>-1</sup>, xenon gas with concentration  $< 5.9$  mg ml<sup>-1</sup> (value corresponding to the pure xenon density at standard temperature and pressure), and barium with concentration 11.2 mg ml<sup>-1</sup>. Another cuvette contained a mixture of one part iodine and two parts barium resulting in a concentration of iodine of 3.3 mg ml<sup>-1</sup> and barium of 7.5 mg ml<sup>-1</sup>. The last cuvette contained a mixture of two parts iodine and one part barium resulting in a concentration of iodine of 6.7 mg ml<sup>-1</sup> and barium of 3.8 mg ml<sup>-1</sup>.

The sample containing multiple contrast elements was used to test the multiple K-edge decomposition capabilities of the system, while barium and iodine mixtures were included to assess the material decomposition in the case of spatially colocalized contrast agents.

### 2.3. Image acquisition, reconstruction and decomposition

A CT scan was acquired for each sample, consisting of 1210 projections over 180° obtained with an exposure time of 200 ms per projection and a frame rate of 4.29 Hz. The sample was scanned in continuous-rotation mode with an angular speed 0.644 deg s<sup>-1</sup>, corresponding to a total scan time of 280 s.

A detector-specific pre-processing procedure, including flat-field normalization, was applied to the projection images before tomographic reconstruction through conventional filtered back projection (Brombal *et al* 2018). For each dataset, the number of reconstructed slices matches the number of illuminated pixel rows, each corresponding to a different energy. The number of illuminated pixel rows is directly proportional to the energy bandwidth achieved in each acquisition.

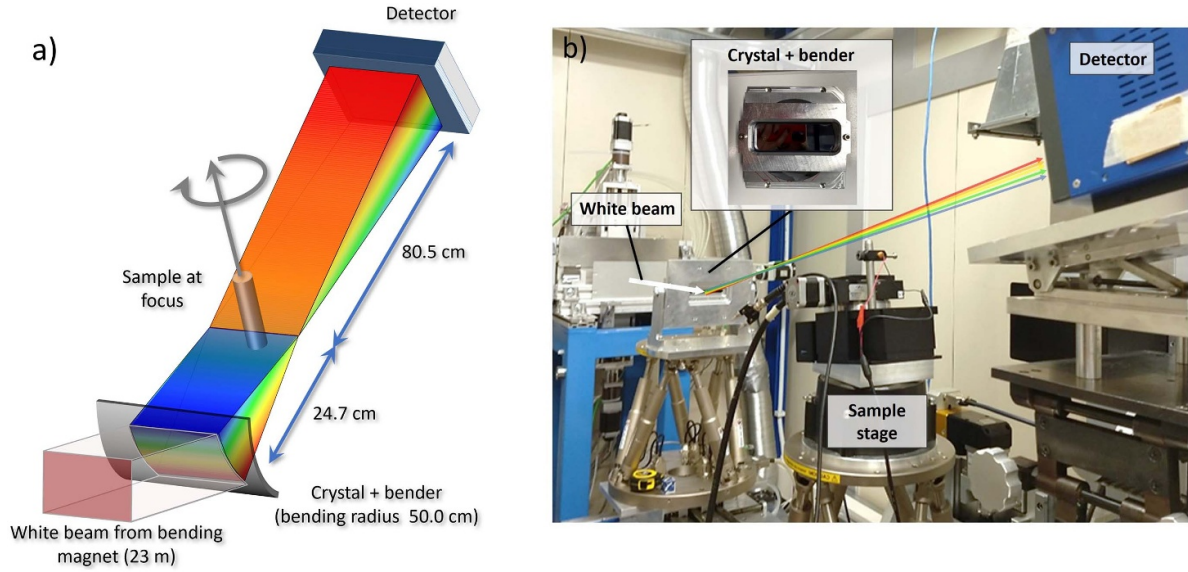


**Figure 1.** Sketch (a) and photo (b) of the experimental setup for the image acquisition. After traversing the crystal, the vertically energy-dispersed beam focuses on the sample and then diverges on the detector. The sample is positioned on the sample stage, at focus.

The SKES material decomposition algorithm was applied to the reconstructed slices to produce the density maps of each element of interest (Zhu *et al* 2014). The algorithm assumes an x-ray beam separated into  $n$  energy levels and an object to scan composed of  $m$  known different materials. Thus, the number of transmitted photons  $N^i$  for the  $i$ th energy is, according to Lambert–Beer’s law:

$$N^i = N_0^i \exp \left( \sum_{j=1}^m - \frac{\mu}{\rho} \Big|_j^i \rho_j t_j \right) \quad (1)$$

where  $N_0^i$  is the incident number of photons,  $\frac{\mu}{\rho} \Big|_j^i$  are the mass attenuation coefficients relative to the  $i$ th energy and the  $j$ th material, and  $t_j$ , where  $j = 1, \dots, m$ , are the material thicknesses. Defining  $S^i$  as follows:

$$S^i = -\ln \left( \frac{N^i}{N_0^i} \right) \quad (2)$$

the following matrix system can be obtained:

$$\begin{pmatrix} S^1 \\ \vdots \\ S^n \end{pmatrix} = \begin{pmatrix} \frac{\mu}{\rho} \Big|_1^1 & \dots & \frac{\mu}{\rho} \Big|_m^1 \\ \vdots & & \vdots \\ \frac{\mu}{\rho} \Big|_1^n & \dots & \frac{\mu}{\rho} \Big|_m^n \end{pmatrix} \begin{pmatrix} \rho_1 t_1 \\ \vdots \\ \rho_m t_m \end{pmatrix}. \quad (3)$$

The mass attenuation coefficients in the matrix are known and can be found in publicly available databases (Hubbell and Seltzer 1996). Therefore, the matrix system is composed of  $n$  equations and  $m$  unknowns, with  $m \leq n$ : by inverting it through a least squares minimization algorithm, for each chosen material the  $\rho \cdot t$  maps, in the case of planar radiography, or the  $\rho$  maps, in the case of tomography, are obtained.

The algorithm can be applied to any set of chosen materials. In biomedical imaging applications, the most common choice consists in the selection of water, of which soft tissues are mostly composed of, and one or more contrast elements that typically target specific anatomical districts. This approach was followed in this paper by selecting specific combinations of silver, iodine, xenon, and barium with water.

As it is clear from equation (3), the decomposition algorithm requires the knowledge of the mass attenuation coefficient matrix, which was calculated using the Matlab function *PhotonAttenuation* (Tuszynski 2023), directly accessing NIST database (Hubbell and Seltzer 1996). In order to achieve a better match between the measured intensity transitions at the K-edge energy and the tabulated mass attenuation coefficient as a function of energy, the latter was smoothed through convolution with a Gaussian function whose full width at half maximum (FWHM) corresponded to the system’s energy resolution (see section 2.4.2). Finally, it should be remarked that, by considering the system’s geometry (i.e. relative distances and effective pixel size), the applied decomposition procedure is inherently quantitative and does not require any density calibration based on objects with known concentrations.

## 2.4. Energy characterization

**2.4.1. Calibration.** The decomposition described in the previous section requires the knowledge of the exact energy level for each row of pixels, i.e. an energy calibration. Through calibration, the correct mass attenuation coefficient values can be inserted in the matrix in equation (3). An analytical method, requiring the knowledge of the geometry of the crystal-detector system and the presence of a well-visible K-edge transition within the FOV, was used to calibrate the images. The energy-position information for every row of

**Table 1.** Summary of energy resolution  $dE$  and energy bandwidth  $\Delta E$  values for each scanned energy. The relative resolution  $dE/E$  and relative bandwidth  $\Delta E/E$  are indicated as well.

Contrast Element	E (keV)	eV/pixel	$dE$ (eV)	$dE/E (\times 10^{-3})$	$\Delta E$ (keV)	$\Delta E/E (\%)$
Silver	25.5	10.6	$56.4 \pm 1.3$	$2.21 \pm 0.05$	$3.44 \pm 0.05$	13.5
Iodine	33.2	18.0	$109.6 \pm 2.2$	$3.30 \pm 0.07$	$4.98 \pm 0.05$	15.0
Xenon	34.6	19.9	$125.0 \pm 6.1$	$3.61 \pm 0.07$	$5.45 \pm 0.03$	15.8
Barium	37.5	22.9	$139.9 \pm 3.6$	$3.73 \pm 0.10$	$5.73 \pm 0.05$	15.3

pixels of the detector can be determined through the following formula (Qi *et al* 2020):

$$E_i = \frac{hc}{2d_{hkl} \sin\left(\theta_K + \frac{1}{2} \tan^{-1}\left(\frac{y_i - y_K}{d_{fd}}\right)\right)} \quad (4)$$

where  $E_i$  is the energy at the  $i$ th pixel row of the detector,  $h$  is the Planck constant,  $c$  is the speed of light,  $d_{hkl}$  is the d-spacing of the crystal,  $\theta_K$  is the Bragg diffraction angle of the x-rays at the K-edge energy,  $d_{fd}$  is the focus-to-detector distance,  $y_K$  is the vertical pixel location of the K-edge energy on the detector and  $y_i$  location of the  $i$ th pixel row. Given the K-edge energy  $E_K$ , the Bragg diffraction angle  $\theta_K$ , that appears in equation (4), is calculated as:

$$\theta_K = \text{asin}\left(\frac{hc}{2E_K d_{hkl}}\right). \quad (5)$$

Hence, the knowledge of the geometrical parameters listed above related to the acquisition system allows the recovery of the energy information from each pixel row.

**2.4.2. Resolution and bandwidth.** Ideally, the intensity transition at the K-edge energy is sharp, and has a width of a few eV due to intrinsic lifetime broadening effects (Nicolas and Miron 2012). In crystal-based spectral systems the energy resolution is typically broader, hence the transition is detected over a wider energy range. The energy resolution of the system was measured by retrieving the intensity profile plot along the energy (i.e. vertical) axis at a position corresponding to the absorption edges. Energy resolutions for silver, iodine, and barium, noted in table 1, were derived from the single-element datasets, while the one of xenon was obtained from the mixed sample dataset. Notably, despite the system being centered on xenon's K-edge energy, the energy resolutions calculated for iodine and barium from the mixed sample dataset produced compatible results. Each profile plot was fitted with the following erf function:

$$f(x) = a + b \cdot \text{erf}\left(\frac{x-c}{d}\right) \quad (6)$$

where  $a$ ,  $b$ ,  $c$ , and  $d$  are the fit parameters, and the variable  $x$  corresponds to energy (see figure 2, panels (a) and (b)). By assuming a Gaussian energy blurring, the FWHM in pixel units is computed as:

$$\text{FWHM} = 2\sqrt{\ln(2)}d. \quad (7)$$

The pixel equivalent in energy was calculated from the energy calibration. By multiplying the energy pixel equivalent and the FWHM estimated as in equation (7), the system's absolute ( $dE$ ) and relative ( $dE/E$ ) energy resolutions are evaluated.

The main parameters that affect the energy bandwidth are the crystal bending radius and the Bragg angle. Both parameters are, as a first approximation, inversely proportional to the bandwidth. While the bending radius remained fixed for all measurements, the Bragg angle was adjusted depending on the contrast element used, in order for the energy spectrum to encompass its K-edge energy.

The Gaussian shape of the incident polychromatic synchrotron beam is maintained after diffracting through the crystal. For this reason, the energy bandwidth  $\Delta E$  for all datasets was measured via a Gaussian fit on the vertical profile plot extracted from the flat field images (see figure 2, panels (c) and (d)). The full width at tenth maximum was chosen as a representative value of the largest portion of the beam, i.e. the largest energy beamwidth that has sufficient flux for imaging purposes. From previous considerations, the relative energy bandwidth ( $\Delta E/E$ ) is expected to be constant.

### 3. Results

The results are organized in two sections. In the first one, the energy characterization of the system in terms of resolution and bandwidth is reported. In the second section, imaging results and contrast media density quantification are outlined both for single-contrast-element samples and for the mixed sample.

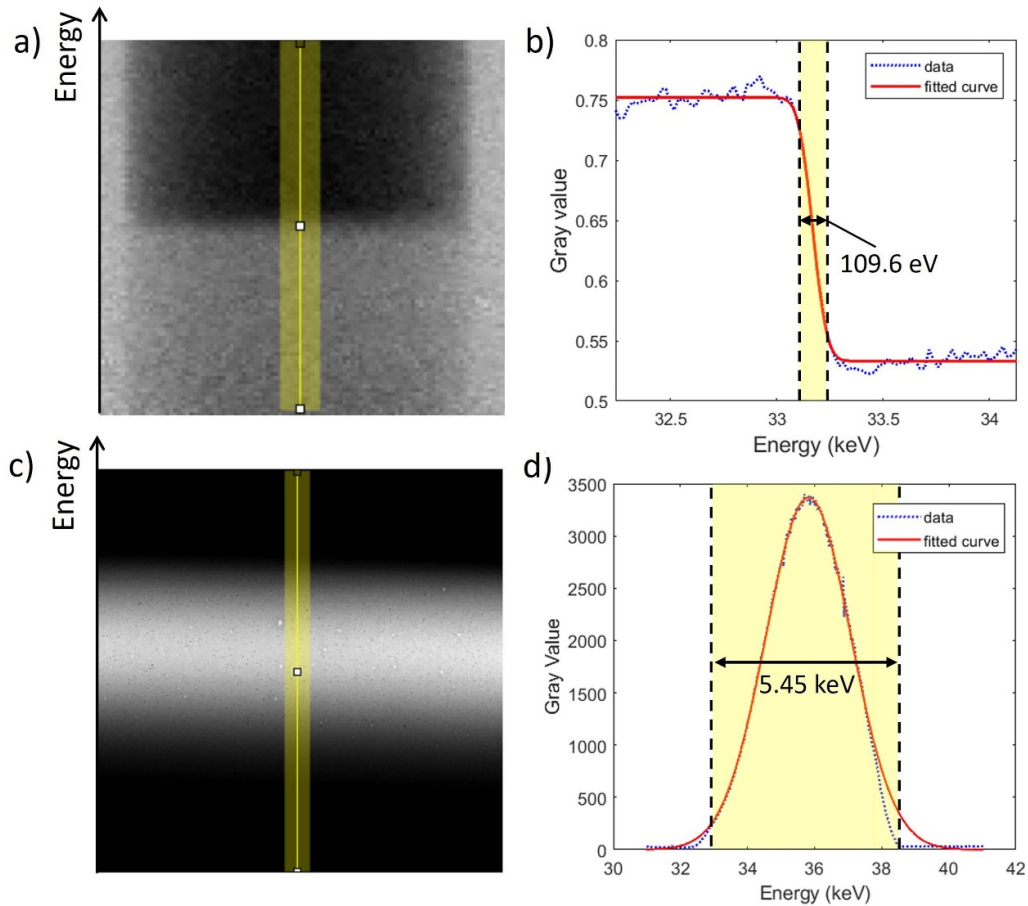
#### 3.1. Energy resolution and bandwidth

Table 1 summarizes the measured values of energy resolution and bandwidth. For the investigated energies, the energy resolution is found to be approximately linear with energy in the range 25.5 to 37.5 keV, as shown in figure 3(right axis), and corresponds to a relative energy resolution around  $3 \times 10^{-3}$ .

As predicted, the measured bandwidth scales with the selected energy, as shown in figure 3(left axis), and corresponds to a relative energy bandwidth of around 15%.

#### 3.2. Contrast media quantification

Either a single-contrast element SKES decomposition or a multiple-contrast element decomposition, according to (3), was applied to the reconstructed slices, depending on the



**Figure 2.** (a) Intensity transition at iodine K-edge energy along with the vertical profile used to measure the energy resolution. (b) Erf function fit performed on the vertical profile plot extracted from (a). (c) Flat image of the vertically energy-dispersed beam centered at Xenon K-edge energy (34.6 keV). The vertical profile used to measure the energy bandwidth is shown. (d) Gaussian fit performed on the vertical profile plot extracted from (c), its FWTM was considered as the value of the energy bandwidth.

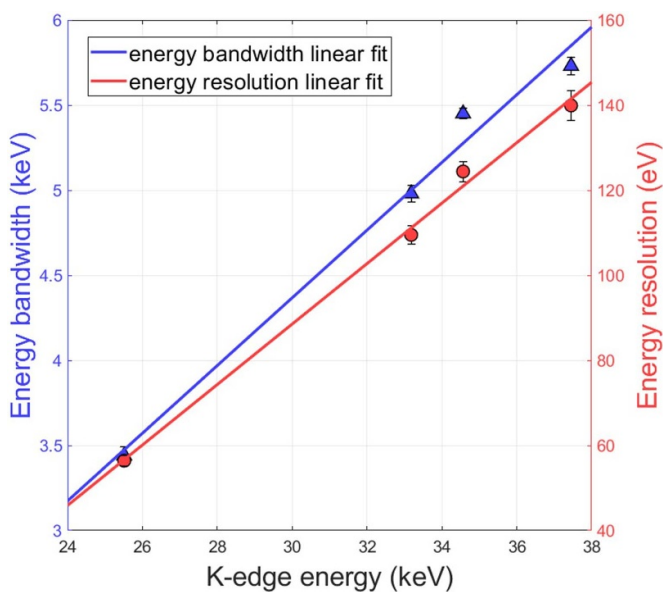


**Figure 3.** Plot of energy bandwidth and energy resolution as a function of K-edge energy and their relative linear fits.

number of contrast elements contained in the sample. The resulting density maps were used to obtain quantitative measurements of the concentrations of the contrast elements. The measurements were performed by selecting a circular region of interest (ROI) inside each cuvette and by measuring its mean intensity. The uncertainty associated with each density measurement is its standard deviation inside the selected ROI. It should be remarked that no calibration fit is used, and density distributions derive uniquely from element decomposition and from the knowledge of the reconstruction voxel size. All images were obtained across a FOV of 5 cm.

**3.2.1. Single-contrast element decomposition.** The density maps from all single-contrast element datasets, containing respectively silver, iodine, and barium, each diluted with water, are shown in figure 4. As expected, water is clearly visible inside all the non-empty cuvettes, in panels (a2)–(c2), with no relevant intensity variation. The contrast elements can be observed in decreasing intensity (i.e. decreasing concentration), in panels (a1)–(c1). The quantitative measurements of

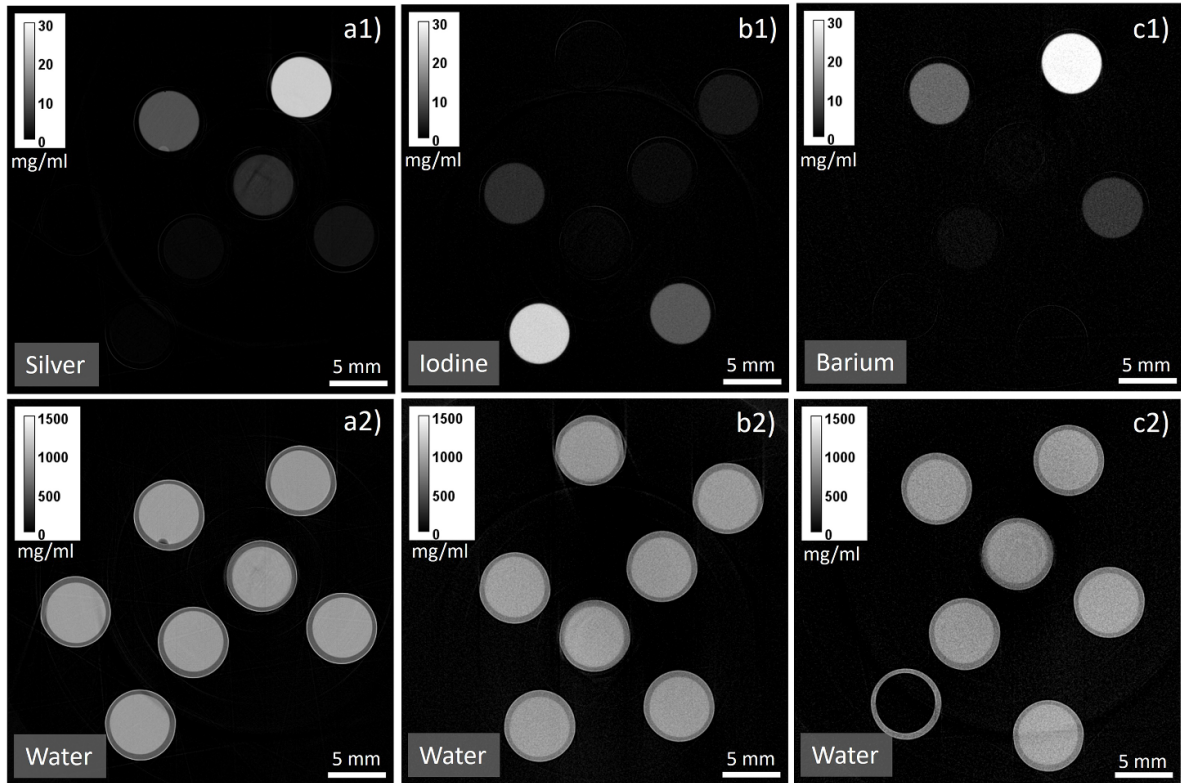


**Figure 4.** Silver (a1), iodine (b1) and barium (c1) SKES decomposition images and their relative water images (a2), (b2) and (c2). In the density maps of the contrast elements, the decreasing concentrations in the cuvettes can be noticed (from brighter to darker).

**Table 2.** Expected and measured densities of silver, iodine, and barium inside the cuvettes. Measurements were made by selecting a ROI in each cuvette and by measuring its average intensity. The uncertainty is determined by the standard deviation within the ROI.

Silver ( $\text{mg ml}^{-1}$ )		Iodine ( $\text{mg ml}^{-1}$ )		Barium ( $\text{mg ml}^{-1}$ )	
Expected	Measured	Expected	Measured	Expected	Measured
25.0	$24.0 \pm 0.2$	25.0	$24.8 \pm 0.5$	28.1	$29.3 \pm 0.8$
10.0	$9.6 \pm 0.2$	10.0	$10.3 \pm 0.4$	11.2	$12.1 \pm 0.8$
5.0	$5.0 \pm 0.4$	5.0	$5.2 \pm 0.4$	5.6	$6.3 \pm 0.8$
2.5	$2.2 \pm 0.2$	2.5	$2.7 \pm 0.4$	1.1	$1.4 \pm 0.7$
1.0	$0.9 \pm 0.2$	1.0	$1.3 \pm 0.4$	0.6	$0.7 \pm 0.8$
0.5	$0.4 \pm 0.2$	0.5	$0.7 \pm 0.5$	0.0	$-0.1 \pm 0.7$
0.0	$-0.1 \pm 0.2$	0.0	$0.3 \pm 0.4$	0.0	$0.0 \pm 0.7$

the contrast element dilutions, measured from the decomposition images, are reported in table 2.

In the case of silver, except for the highest concentration, which is underestimated by about 4%, all the measurements are compatible with the expected value within three standard deviations. Within the error bars, the iodine dataset reveals that the system allows good quantitative determination of all the given material densities. The barium measurements appear slightly systematically overestimated (the highest concentration of about 4%) compared to the nominal ones. Nevertheless, the ratio between consecutive pairs of densities is approximately correct, so there is proportionality between expected and measured densities. The overestimation is therefore possibly due to an error in the nominal density of the stock solution,

which was used to prepare all the working solutions. The root-mean-square-errors (RMSE) of the measured concentrations with respect to the expected values are  $0.45 \text{ mg ml}^{-1}$ ,  $0.25 \text{ mg ml}^{-1}$ ,  $0.73 \text{ mg ml}^{-1}$  for silver, iodine and barium, respectively. Their relative RMSE (RRMSE) are 1.6%, 2.4%, 0.9%, respectively.

The negative density values reported in the table are a result of the decomposition algorithm, which simply involves matrix inversion without any constraints applied, and the presence of noise in the images. Accordingly, values which ideally should be zero fluctuate, hence they can also take negative values. It is important to note that, in all datasets, even the smallest concentration considered ( $0.5 \text{ mg ml}^{-1}$ ) is perceived by the imaging system after decomposition. Moreover, it is worth



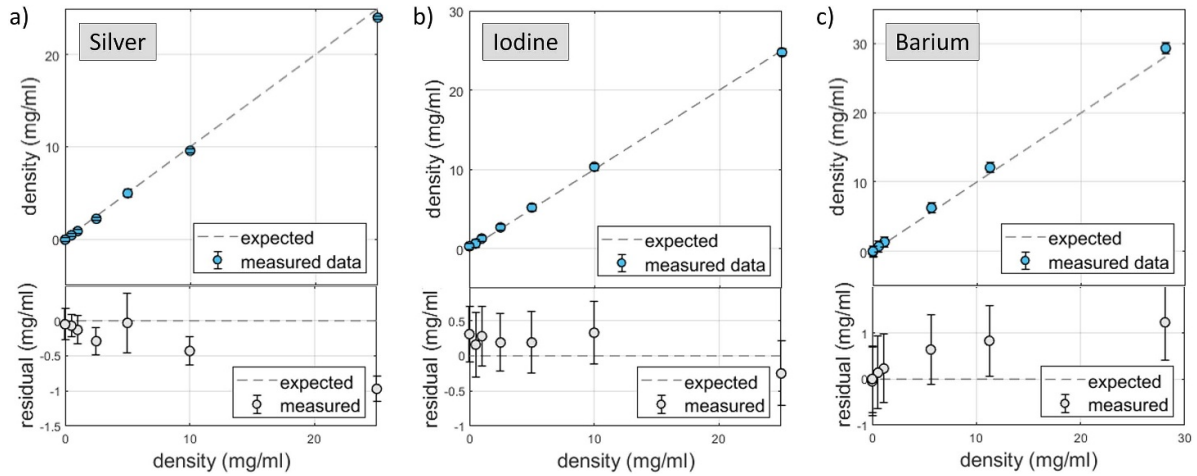


**Figure 5.** Comparison between the expected densities and the measured densities for the three single-contrast-element datasets, and their residuals. Each plotted error is the uncertainty associated to its measurement (corresponding to the standard deviation), as detailed in table 2.

noticing that decomposition is achieved with small image noise, corresponding to density fluctuations in the order of  $0.2 \text{ mg ml}^{-1}$ ,  $0.4 \text{ mg ml}^{-1}$ ,  $0.8 \text{ mg ml}^{-1}$  for silver, iodine, and barium, respectively. The image noise increase at higher energies is primarily governed by the steep decrease in the photon flux at higher energies due to the low critical energy (3.2 keV for storage ring electron energy of 2.0 GeV) of the Elettra synchrotron.

Figure 5 shows a comparison between the expected and measured data for the three datasets described above, along with their respective residuals. Except for the cuvette containing the highest silver concentration, the residual plots show that the measurements are all compatible with the expected densities within three standard deviations.

**3.2.2. Multiple material decomposition.** Owing to the achievement of a large energy bandwidth (5.5 keV), simultaneous imaging of three K-edges (iodine at 33.2 keV, xenon at 34.6 keV and barium at 37.5 keV) was accomplished. By applying the multiple-material decomposition on the dataset, four independent density maps are generated for iodine, xenon, barium, and water, respectively, as shown in figure 6.

The measurements of the three contrast elements, reported in table 3, are all in good agreement with the nominal values considering the error bars. It should be noted that the density of xenon (cuvette 5) is uncertain as the pressure of xenon inside the cuvette was unknown. Nevertheless, since the cuvette was filled at atmospheric pressure, the upper-density limit of xenon is  $5.6 \text{ mg ml}^{-1}$  (pure xenon).

The RMSE of the measured concentrations with respect to the expected values are  $0.24 \text{ mg ml}^{-1}$ ,  $0.76 \text{ mg ml}^{-1}$  for iodine and barium, respectively. Their RRMSE are 1.9%, 5.4%, respectively.

Similarly to the single-contrast element decomposition, the density measurements of barium in cuvettes 2, 3, and 4 are slightly overestimated compared to the expected values. This supports the idea that the concentration of the stock solution

was higher than expected. Additionally, iodine and barium maps in panels (a) and (c) of figure 6 demonstrate that the multi-material SKES allows for the correct quantitative reconstruction of different co-localized contrast media.

In this dataset, the decomposition images are generally noisier (average noise  $> 1 \text{ mg ml}^{-1}$ ) compared to the single-contrast element ones (average noise  $< 1 \text{ mg ml}^{-1}$ ). This is due to two reasons. Firstly, the larger number of unknowns that appear in the matrix system equation (3) increases the decomposition noise (Di Trapani *et al* 2022). Additionally, noise is influenced by the effect of the gaussian-shaped vertical intensity distribution of the beam coupled with its peculiar vertical energy dispersion (see figure 2). With an energy bandwidth of 5.5 keV, centered approximately at the energy of the xenon K-edge, the iodine and the barium K-edges are localized, respectively, in the leading and falling slope of the vertical intensity distribution. In this region, the photon flux is considerably lower and, subsequently, the associated relative stochastic noise is higher compared to the central region. Therefore, the noise in a specific material decomposition image increases when the material's K-edge in the projections is located on the slopes of the intensity distribution of the beam, corresponding to smaller photon fluxes. This explains why the xenon images (whose K-edge is positioned on the maximum of the Gaussian) feature the lowest noise, while the location of the iodine and barium K-edges yields noisier decomposition images. Nonetheless, the noise level is in all cases below  $2 \text{ mg ml}^{-1}$ , which can be regarded as a small value considering typical contrast media concentrations in biomedical applications.

Figure 7(a) shows a composite image where the contrast media are coded in RGB channels, displaying densities of iodine (red), xenon (green) and barium (blue), respectively. Figure 7(b) graphically shows a comparison between the expected and measured densities inside each cuvette, following the cuvette order indicated in figure 7(a).

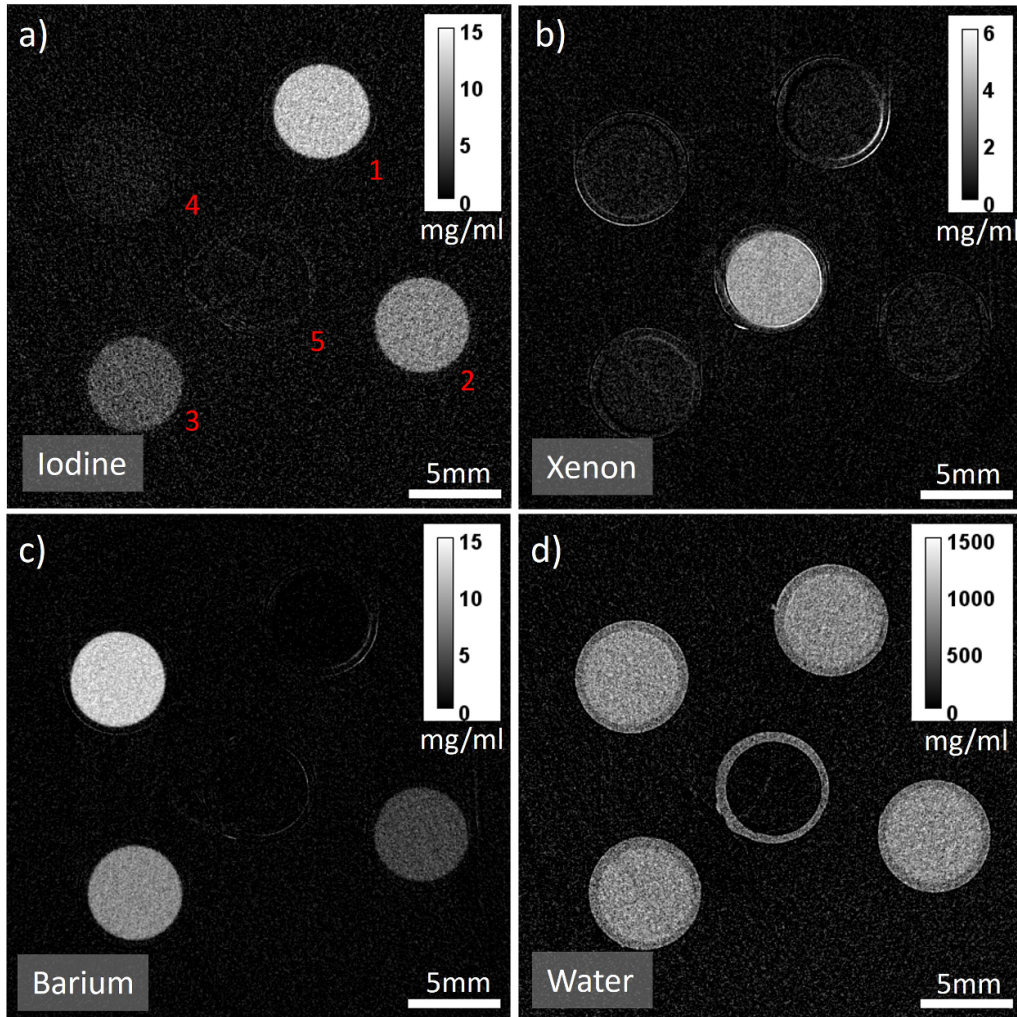


**Figure 6.** Iodine (a), xenon (b), barium (c), and water (d) density maps obtained through the multiple-material decomposition. The cuvettes are numbered in the following order: (1) iodine  $10.0 \text{ mg ml}^{-1}$ , (2) and (3) mixtures of iodine and barium, (4) barium  $11.2 \text{ mg ml}^{-1}$ , (5) Xenon.

**Table 3.** Expected and calculated densities of iodine, xenon, and barium inside the cuvettes. Measurements were made by selecting a ROI in each cuvette and by measuring its average intensity. The uncertainty is determined by the standard deviation within the ROI. The measurements are displayed following the numerical order indicated on panel (a) of figure 6.

Cuvette No.	Iodine ( $\text{mg ml}^{-1}$ )		Xenon ( $\text{mg ml}^{-1}$ )		Barium ( $\text{mg ml}^{-1}$ )	
	Expected	Measured	Expected	Measured	Expected	Measured
1	10.0	$10.3 \pm 1.7$	0.0	$0.0 \pm 0.6$	0.0	$-0.2 \pm 1.1$
2	6.7	$6.8 \pm 1.9$	0.0	$0.0 \pm 0.6$	3.8	$4.2 \pm 1.1$
3	3.3	$3.6 \pm 1.9$	0.0	$0.2 \pm 0.6$	7.5	$8.5 \pm 1.1$
4	0.0	$0.1 \pm 1.8$	0.0	$0.2 \pm 0.6$	11.2	$12.5 \pm 1.2$
5	0.0	$0.2 \pm 1.8$	$\leq 5.6$	$3.6 \pm 0.5$	0.0	$0.0 \pm 1.0$

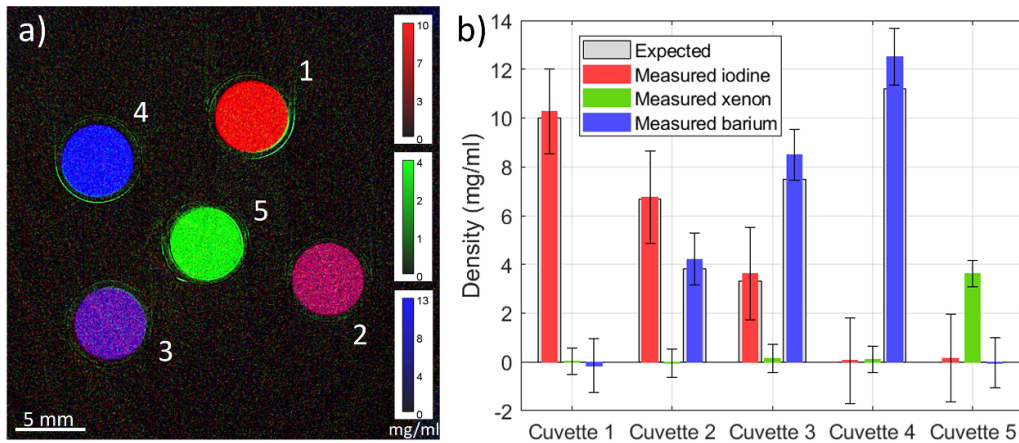


**Figure 7.** (a) Composite image of iodine (red), xenon (green), and barium (blue) densities in three RGB channels. (b) Comparison between the expected and measured densities inside the cuvettes. Each plotted error is the uncertainty associated to its measurement (corresponding to the standard deviation), as detailed in table 2.

#### 4. Discussion and conclusions

The novel SKES system implemented at the SYRMEP beamline at Elettra has been characterized in terms of its energy resolution and energy bandwidth, and tested on biologically-relevant contrast media. Large energy bandwidths ( $\sim 15\%$ ) at relative energy resolutions of the order of  $3 \times 10^{-3}$  have been consistently achieved across energies ranging from 25 keV to 38 keV.

In general, both the energy bandwidth and the energy resolution are influenced by multiple crystal parameters, including the reflection type, the curvature radius, and the thickness, as well as various x-ray beam parameters, the most important being the source divergence (Qi *et al* 2021).

In this framework, it is interesting to compare the results herein presented with previous studies. Taking as a reference the iodine K-edge, an energy resolution of 109.6 eV FWHM and a bandwidth of 4.98 keV (see table 1) were obtained. For comparison, the original work introducing the SKES by Zhu *et al* (2014) reported a 3-times better energy resolution (32.6 eV FWHM), but at the expense of a 9-times smaller energy bandwidth (0.56 keV). These results were obtained by employing the  $\langle 311 \rangle$  reflection of a  $600 \mu\text{m}$  thick Si crystal curved to a 1 m bending radius. More recently, by using the  $\langle 111 \rangle$  reflection of a  $600 \mu\text{m}$  thick crystal curved to 1 m bending radius, Bassey *et al* (2016) reported an energy resolution of 48.8 eV FWHM and a wide bandwidth reaching 15.0 keV. This extreme bandwidth was reached by exploiting the horizontal beam divergence (order of  $10^{-3}$  rad), that is one order of magnitude larger than the vertical divergence (order of  $10^{-4}$  rad) in the case of bending magnet sources. This geometry implies that, at the focus position, the useful beam dimension for imaging is determined by the smaller vertical divergence, resulting in a FOV of  $\sim 6$  mm. A FOV this small does not allow, for instance, to perform tomographic imaging of large samples (e.g. small animal studies). Conversely, the  $\sim 5$  keV bandwidth reported in this work was obtained across the vertical direction, exploiting the large-

divergence horizontal direction for imaging. This guarantees a large FOV (50 mm in this work, but can reach 150 mm at the SYRMEP beamline): to the best of the authors' knowledge, this is largest energy-bandwidth reported so far over a several-centimeter FOV, making the system suitable for biomedical imaging applications.

All single-contrast element decomposition images proved to be quantitatively accurate, yielding sensitivity to very low contrast element concentrations, down to  $0.5 \text{ mg ml}^{-1}$ . The sensitivity of SKES in the case of a multiple-component sample was also assessed. The results show that all contrast elements inside the sample, namely iodine (33.2 keV), xenon (34.6 keV), and barium (37.5 keV), were accurately resolved, even when the elements were spatially co-localized. The latter paves the way for the application of multiple SKES to achieve simultaneous quantitative imaging of different anatomical districts or to enhance functional imaging (Ashton *et al* 2015, Yeh *et al* 2017). Specifically, considering the simultaneous use of iodine, xenon, and barium, cardiovascular, pulmonary (Giacomini *et al* 1998) and gastrointestinal/inflammatory (Dullin *et al* 2015) imaging applications with a single scan can be envisaged on biological samples both *ex-vivo* and *in-vivo*.

Further efforts will be devoted to enhance energy resolution, aiming towards large FOV x-ray absorption spectroscopy applications. This will require the modification of crystal parameters including its thickness, reflection type, and bending radius. Similar measurements based on dispersive bent crystals have been previously conducted at different synchrotron facilities (Matsushita and Phizackerley 1981, Katayama *et al* 2015), although they were limited by an energy bandwidth below 1 keV. Additionally, contrast medium sensitivity at levels encountered in molecular imaging ( $< 100 \mu\text{g ml}^{-1}$ ) will be explored. This will involve the increase of the system efficiency and the refinement of the decomposition algorithm. The first will involve the optimization of the crystal's parameters based on the energy range of interest, while the second will require the development of dedicated de-noising strategies.

## Data availability statement

The data that support the findings of this study are openly available at the following URL/DOI: <https://doi.org/10.15161/oar.it/143142> (Perion *et al* 2023).

## Acknowledgment

This work has been carried out in the frame of the KISS and SPHERE-X projects, supported by the Istituto Nazionale di Fisica Nucleare (INFN), National Scientific Commission 5 for Technological and Inter-disciplinary Research. The authors are indebted to Dean Chapman and Nazanin Samadi for the numerous discussions and sharing ideas regarding SKES. We express our gratitude to Diego Dreossi, Nicola Sodini, and Adriano Contillo for their help in setting up the SYRMEP beam line.

## ORCID iDs

P Perion  <https://orcid.org/0009-0008-1378-5288>

L Brombal  <https://orcid.org/0000-0002-4009-8191>

P Oliva  <https://orcid.org/0000-0002-9446-3967>

## References

- Altman A and Carmi R 2009 Tu-e-210a-03: a double-layer detector, dual-energy CT - principles, advantages and applications *Med. Phys.* **36** 2750
- Ashton J R, West J L and Badea C T 2015 *In vivo* small animal micro-CT using nanoparticle contrast agents *Front. Pharmacol.* **6** 256
- Badea C T, Clark D P, Holbrook M, Srivastava M, Mowery Y and Ghaghada K 2019 Functional imaging of tumor vasculature using iodine and gadolinium-based nanoparticle contrast agents: a comparison of spectral micro-CT using energy integrating and photon counting detectors *Phys. Med. Biol.* **64** 065007
- Ballabriga R *et al* 2016 Review of hybrid pixel detector readout ASICs for spectroscopic X-ray imaging *J. Inst.* **11** P01007
- Bassey B, Martinson M, Samadi N, Belev G, Karanfil C, Qi P and Chapman D 2016 Multiple energy synchrotron biomedical imaging system *Phys. Med. Biol.* **61** 8180
- Bayat S *et al* 2001 Quantitative functional lung imaging with synchrotron radiation using inhaled xenon as contrast agent *Phys. Med. Biol.* **46** 3287
- Bellazzini R, Spandre G, Brez A, Minuti M, Pinchera M and Mozzo P 2013 Chromatic x-ray imaging with a fine pitch CDTE sensor coupled to a large area photon counting pixel asic *J. Instrum.* **8** C02028
- Bertrand B *et al* 2005 Comparison of synchrotron radiation angiography with conventional angiography for the diagnosis of in-stent restenosis after percutaneous transluminal coronary angioplasty *Eur. Heart J.* **26** 1284–91
- Brombal L, Arfelli F, Menk R H, Rigon L and Brun F 2023 Pepi lab: a flexible compact multi-modal setup for x-ray phase-contrast and spectral imaging *Sci. Rep.* **13** 4206
- Brombal L, Donato S, Brun F, Delogu P, Fanti V, Oliva P, Rigon L, Di Trapani V, Longo R and Golosio B 2018 Large-area single-photon-counting CdTe detector for synchrotron radiation computed tomography: a dedicated pre-processing procedure *J. Synchrotron Radiat.* **25** 1068–77
- Brun F *et al* 2020 Single-shot k-edge subtraction x-ray discrete computed tomography with a polychromatic source and the pixie-iii detector *Phys. Med. Biol.* **65** 055016
- Delogu P, Oliva P, Bellazzini R, Brez A, de Ruvo P, Minuti M, Pinchera M, Spandre G and Vincenzi A 2016 Characterization of pixirad-1 photon counting detector for x-ray imaging *J. Instrum.* **11** 01015–01015
- Di Trapani V, Brombal L and Brun F 2022 Multi-material spectral photon-counting micro-CT with minimum residual decomposition and self-supervised deep denoising *Opt. Express* **30** 42995–3011
- Dullin C *et al* 2015 Functionalized synchrotron in-line phase-contrast computed tomography: a novel approach for simultaneous quantification of structural alterations and localization of barium-labelled alveolar macrophages within mouse lung samples *J. Synchrotron Radiat.* **22** 143–55
- Fredenberg E 2018 Spectral and dual-energy x-ray imaging for medical applications *Nucl. Instrum. Methods Phys. Res. A* **878** 74–87
- Giacomini J *et al* 1998 Bronchial imaging in humans using xenon k-edge dichromography *Nucl. Instrum. Methods Phys. Res. A* **406** 473–8
- Hubbell J H and Seltzer S M 1996 tables of x-ray mass attenuation coefficients and mass energy-absorption coefficients 1 keV to 20 MeV for elements  $Z = 1$  to 92 and 48 additional substances of dosimetric interest *Technical Report* National Institute of Standards and Technology (NIST)
- Katayama M, Miyahara R, Watanabe T, Yamagishi H, Yamashita S, Kizaki T, Sugawara Y and Inada Y 2015 Development of dispersive xafs system for analysis of time-resolved spatial distribution of electrode reaction *J. Synchrotron Radiat.* **22** 1227–32
- Martinson M, Samadi N, Bassey B, Gomez A and Chapman D 2015 Phase-preserving beam expander for biomedical x-ray imaging *J. Synchrotron Radiat.* **22** 801–6
- Matsushita T and Phizackerley R P 1981 A fast x-ray absorption spectrometer for use with synchrotron radiation *Jaapn. J. Appl. Phys.* **20** 2223
- Nicolas C and Miron C 2012 Lifetime broadening of core-excited and -ionized states *J. Electron Spectrosc. Relat. Phenom.* **185** 267–72
- Panahifar A, Samadi N, Swanston T M, Chapman L D and Cooper D M 2016 Spectral k-edge subtraction imaging of experimental non-radioactive barium uptake in bone *Phys. Medica* **32** 1765–70
- Panta R, Bell S, Healy J, Aamir R, Bateman C, Moghiseh M, Butler A and Anderson N 2018 Element-specific spectral imaging of multiple contrast agents: a phantom study *J. Instrum.* **13** T02001
- Perion P, Brombal L, Delogu P, Trapani D, Vittorio M, Hendrik R, Oliva P and Arfelli F 2023 A high sensitivity wide bandwidth spectral system for multiple K-edge imaging: data (<http://doi.org/10.15161/oar.it/143142>)
- Qi P, Samadi N and Chapman D 2020 X-ray spectral imaging program: XSIP *J. Synchrotron Radiat.* **27** 1734–40
- Qi P, Samadi N, Martinson M, Ponomarenko O, Bassey B, Gomez A, George G N, Pickering I J and Chapman L D 2019 Wide field imaging energy dispersive x-ray absorption spectroscopy *Sci. Rep.* **9** 1–14
- Qi P, Shi X, Samadi N and Chapman D 2021 Bent Laue crystal anatomy: new insights into focusing and energy-dispersion properties *J. Appl. Crystallogr.* **54** 409–26
- Rajendran K *et al* 2022 First clinical photon-counting detector CT system: technical evaluation *Radiology* **303** 130–8
- Rubenstein E 1984 Medical imaging with synchrotron radiation *Nucl. Instrum. Methods Phys. Res.* **222** 302–7
- Samadi N, Martinson M, Bassey B, Gomez A, Belev G and Chapman D 2016 An energy dispersive bent laue

- monochromator for K-edge subtraction imaging *AIP Conf. Proc.* **1741** 040004
- Thomlinson W, Elleaume H, Porra L and Suortti P 2018 K-edge subtraction synchrotron x-ray imaging in bio-medical research *Phys. Medica* **49** 58–76
- Tromba G *et al* 2010 The symep beamline of elettra: clinical mammography and bio-medical applications *AIP Conf. Proc.* **1266** 18–23
- Tuszynski J 2023 Photonattenuation (available at:[www.mathworks.com/matlabcentral/fileexchange/12092-photonattenuation](http://www.mathworks.com/matlabcentral/fileexchange/12092-photonattenuation)) (Accessed 29 August 2023) MATLAB Central File Exchange
- Vries A, Roessl E, Kneepkens E, Thran A, Brendel B, Martens G, Proska R, Nicolay K and Gröll H 2014 Quantitative spectral K-edge imaging in preclinical photon-counting x-ray computed tomography *Investigative Radiol.* **50** 297–304
- Yeh B M *et al* 2017 Opportunities for new CT contrast agents to maximize the diagnostic potential of emerging spectral CT technologies *Adv. Drug. Deliv. Rev.* **113** 201–22
- Zhu Y, Samadi N, Martinson M, Basseby B, Wei Z, Belev G and Chapman D 2014 Spectral K-edge subtraction imaging *Phys. Med. Biol.* **59** 2485–503